

A systematic dataset generation technique applied to data-driven automotive aerodynamics

Mark Benjamin and Gianluca Iaccarino

August 15, 2024

Abstract

A novel strategy for generating datasets is developed within the context of drag prediction for automotive geometries using neural networks. A primary challenge in this space is constructing a training database of sufficient size and diversity. Our method relies on a small number of starting data points, and provides a recipe to interpolate systematically between them, generating an arbitrary number of samples at the desired quality. We test this strategy using a realistic automotive geometry, and demonstrate that convolutional neural networks perform exceedingly well at predicting drag coefficients and surface pressures. Promising results are obtained in testing extrapolation performance. Our method can be applied to other problems of aerodynamic shape optimization.

1 Introduction

1.1 Motivation

The computation of aerodynamic drag is an expensive component of automotive design, requiring one computational fluid dynamics simulation per design point. It is also an essential component of the design process; since drag force is quadratic in vehicle velocity, it becomes the dominant mode of energy loss at high speed, affecting vehicle top speed, fuel efficiency and stability. The complexity of modern vehicle designs leads to a high-dimensional parameter space that can be prohibitively expensive to sample. In addition, the evaluation of the quantity of interest — the drag coefficient — for each single design point is costly, requiring the solution of the Navier-Stokes equations at high Reynolds numbers, on a mesh sufficiently fine so as to resolve the details of the automotive design. Surrogate models are therefore of interest; in particular, given the nature of the governing equations and the complexity of the geometries of interest, one seeks data-driven models for drag prediction. The drag coefficient depends on flow and geometry parameters; in our study the flow parameters are fixed; thus, the model learns a mapping between the automotive geometry and the drag coefficient.

The primary issue with constructing data-driven models in this application space is the paucity of freely-available, realistic automotive geometries, owing primarily to the proprietary nature of commercial designs. A compounding factor is the nature of the automotive design process, which is driven by not just aerodynamic efficiency in mind but with other (and sometimes conflicting) considerations such as aesthetics, regulatory compliance, and manufacturability. (This is in contrast with, say, airplane wing design, where (regulatory compliance and manufacturability notwithstanding) the design process is far more organic: one begins with a cross-section of an airfoil with the desired drag and lift characteristics, then the wing is extruded in the third dimension based on loading characteristics.) In practice, the design problem for the aerodynamicist involves limited scope; small variations in a discrete number of parameters. As an example, the aerodynamicist will never be able to redesign the Ford Mustang to have the same drag coefficient as, say, a Tesla Model S (which is one of the only passenger cars whose exterior design was driven primarily by aerodynamics [19]), because a Ford Mustang's overall shape and first order drag characteristics are dictated by the need to look like a Ford Mustang, for aesthetic appeal. This design paradigm makes it all the more important to have a rich and variegated training set, because it is the details on a scale much smaller than the characteristic length scale of the vehicle that one has the freedom to modify with the aim of improving aerodynamics. In the absence of a sufficiently large and diverse training set, models suffer in accuracy and predictive capability. In

this work, we develop a methodology of generating geometries for training in a controlled manner, starting with a small number of starting cases. By generating a dataset with sufficient granularity, we show that data-driven model predictions show excellent predictive capabilities for quantities of interest at different levels of abstraction – scalar (the drag coefficient), vector (the surface pressure along the axis of symmetry), and tensor (the surface pressure on the wetted area).

1.2 Geometry parameterization and dataset generation

There have been attempts in the literature to address the issue of dataset generation in aerodynamics problems. Viquerat *et al.* [26] studied the problem of 2D airfoils in the laminar (Re 10) regime, and used a random process to generate Bézier curves with which airfoils were developed. Their approach — which used an immersed boundary solver — showed the importance of having sufficiently variety in the training set, but is not directly translatable to the 3D, fully-turbulent automotive design problem for reasons described earlier, as one does not typically encounter realistic designs through a randomized morphing process. Song *et al.* [23] used the versatile ShapeNet database, which is a large repository of freely-available CAD models organized hierarchically, in their investigations of automotive drag. The database includes several thousand automobile models of varying level of detail and quality. They then trained CNNs with planar images of the inputs to predict the drag coefficient. However, owing to the uncontrolled nature of the dataset, the model had limited predictive success. The use of a database like ShapeNet, while appealing from the perspective of quantity and variety of data, introduces limitations simply by the models not being from sources connected with automotive design and simulation. In the complex realm of automotive design, there is a lack of clarity on the additional coverage in the feature space provided when a new geometry is considered, owing to the nominally high-dimensional parameter space that the designs live in. This also leads to confusion over whether predictions made by models trained on these datasets are actually interpolations or extrapolations. Garcia-Fernandez *et al.* [9] studied simplified representations of heavy vehicles, using CNNs to predict aerodynamic quantities of interest. They followed a similar approach to the other works above, with a manual parameterization of the Ahmed body to generate a training set. Other parameterizations explored in the literature is the idea of using a PolyCube map to represent the geometry [25], or using parameterized curves to generate two-dimensional silhouettes of cars [11], both of which require manual parameterization, and have been tested on relatively simple shapes.

Virtually all the existing work in the literature uses RANS (Reynolds-Averaged Navier-Stokes) simulation data as the ground truth to train the data-driven models. While RANS simulations have been the workhorse for engineering CFD, it has two primary limitations: the extreme mesh requirements for grid-independent solutions in complex geometries, and the inability to capture inherently unsteady phenomena, such as the strong separation seen in the wake of a flow past a bluff automotive body. For these reasons, we use wall-modeled large-eddy simulations (WMLES) to generate the flow solutions. Recent advances in this modeling approach have made cost of accurate solutions of first-order mean quantities at cost comparable with RANS simulations in complex flows of practical relevance [4].

2 Methodology

In this section, we describe the dataset generation method we propose. The goal is to go from a handful of starting geometries, and use them to generate several more in a controlled manner. This is done by constructing the convex hull of the signed distance functions (SDFs) of their surfaces. We use the simplest form of interpolation: barycentric, to generate the convex hull. Finally, we require that the process be bi-directional; i.e. the format of the projections (intermediate geometries) is the same as that of the bases cases. Each step in this process is described in detail below.

2.1 Geometry representation

We begin with a discretized, representation of the geometry, in the stereolithographic (STL) format. The unstructured nature of this format makes generation of new geometries by interpolation between basis cases challenging due to the absence of consistent mapping of corresponding points or features. However, an STL representation is more readily compatible with unstructured CFD solvers, so we introduce an intermediate

transformation to a structured representation, and return to the STL format after any interpolation is performed. To do this, we develop a ray-tracing tool, the working of which is as follows:

- **Structured mesh initialization:** The bounding box $[x_{\min}, x_{\max}] \times [y_{\min}, y_{\max}] \times [z_{\min}, z_{\max}]$ is determined for the STL tessellation \mathcal{T} by evaluating the axis-aligned bounds of all triangles $\{\Delta_i = (\mathbf{v}_1^i, \mathbf{v}_2^i, \mathbf{v}_3^i) \mid i \in \{1, \dots, M\}\}$, where M is the total number of triangles in the STL tessellation, and $\mathbf{v}_1^i, \mathbf{v}_2^i, \mathbf{v}_3^i \in \mathbb{R}^3$ are the vertices of the i -th triangle. The bounding box is discretized into a structured Cartesian grid \mathbb{G} with dimensions $N_x \times N_y \times N_z$, where each N_i is the desired discretization resolution along each axis. It is straightforward to apply a localized refinement in discretization in regions where finer features need to be captured, but for simplicity, we use a uniform discretization resolution in the whole domain in this study.
- **Ray-tracing:** A set of rays $\mathbf{r}(t) = \mathbf{o} + t\mathbf{d}$ is generated along each principal axis (x, y, z), where \mathbf{o} is the ray origin and \mathbf{d} is the unit direction vector aligned with the axis. The ray origins are placed at the centers of the bounding box faces, thus the total number of rays cast is $N_x \times N_y \times N_z$. For each ray $\mathbf{r}(t)$, the algorithm evaluates possible intersections with each triangle $\Delta_i \in \mathcal{T}$. The intersection test utilizes the Möller–Trumbore algorithm [17] to determine if and where the ray intersects the triangle, producing an intersection point \mathbf{p} when a hit is detected.
- **Intersect attribution:** Once an intersection point $\mathbf{p} = (p_x, p_y, p_z)$ is detected, it is mapped onto the corresponding grid cell in \mathbb{G} . The normalized coordinates

$$\tilde{\mathbf{p}} = \left(\frac{p_x - x_{\min}}{x_{\max} - x_{\min}}, \frac{p_y - y_{\min}}{y_{\max} - y_{\min}}, \frac{p_z - z_{\min}}{z_{\max} - z_{\min}} \right)$$

are scaled to obtain the voxel indices (i, j, k) :

$$(i, j, k) = \lfloor \tilde{\mathbf{p}} \cdot (N_x - 1, N_y - 1, N_z - 1) \rfloor,$$

where the floor function $\lfloor \cdot \rfloor$ converts the continuous coordinates to discrete indices. The intersection grids from ray-tracing along all three principal axes are combined to yield a final binary grid $\mathbb{B} \in \{0, 1\}^{N_x \times N_y \times N_z}$, where each cell is defined by:

$$\mathbb{B}_{i,j,k} = \begin{cases} 1 & \text{if } \exists \mathbf{r}(t) \cap \Delta_i \quad \text{s.t. } (i, j, k) = \lfloor \frac{\mathbf{p} - \mathbf{x}_{\min}}{\Delta_x} \rfloor, \\ 0 & \text{otherwise.} \end{cases}$$

Here, $\mathbb{B}_{i,j,k}$ represents whether voxel (i, j, k) in the grid contains part of the geometry (1) or is empty (0). This transformation yields a discrete voxelized representation of the continuous STL geometry \mathcal{T} within the structured grid \mathbb{G} .

Figure 1 shows an example of the binary representation of an example geometry of a car, at a ray-tracing resolution of 1024^3 . Every 5th intersection is shown.

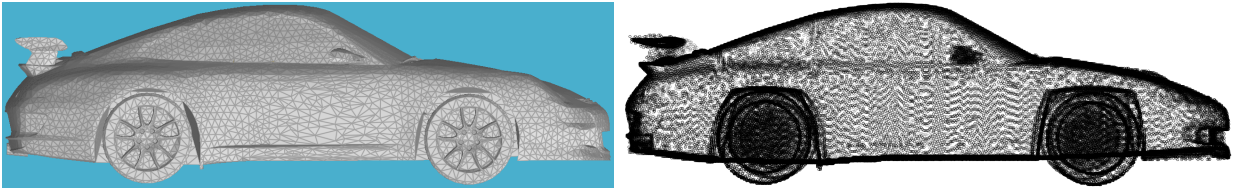


Figure 1: Left: Original STL; right: binary representation

2.2 Geometry interpolation

With the binary representations constructed as above, we next look at the question of interpolating between n given geometries, $\mathbb{B}_{i,j,k}^1, \mathbb{B}_{i,j,k}^2, \dots, \mathbb{B}_{i,j,k}^n$. To accomplish this, we first convert the binary grids into Signed

Distance Functions (SDFs), enabling a continuous representation of the geometries. For all binary grids $\mathbb{B}_{i,j,k}^i$, a hole-filling operation is applied to remove internal voids that are not connected to the boundary of the grid. This involves first dilating the complement of the binary grid $\overline{\mathbb{B}}_{i,j,k}^i = 1 - \mathbb{B}_{i,j,k}^i$:

$$\mathcal{D}^n[\overline{\mathbb{B}}_{i,j,k}^i],$$

where \mathcal{D}^n represents the dilation operation iterated n times. The hole-filled grid is then the complement of this dilated result:

$$\tilde{\mathbb{B}}_{i,j,k}^i = 1 - \mathcal{I}[\mathcal{D}^n[\overline{\mathbb{B}}_{i,j,k}^i]],$$

where \mathcal{I} represents the invasion step, which identifies the regions that cannot be reached from the image boundary. For the filled binary grid $\tilde{\mathbb{B}}_{i,j,k}^i$, the Signed Distance Function (SDF) $\phi_{i,j,k}^i$ is computed as the difference between the distance transform of the exterior and interior regions:

$$\phi_{i,j,k}^i = d(1 - \tilde{\mathbb{B}}_{i,j,k}^i) - d(\tilde{\mathbb{B}}_{i,j,k}^i),$$

where $d(\cdot)$ represents the Euclidean distance transform. The first term calculates the distance to the nearest external boundary, and the second term calculates the distance to the nearest internal boundary. The SDF $\phi_{i,j,k}^i$ thus yields positive values inside the geometry, negative values outside, and zero at the surface. The interpolation involves constructing the convex hull of the basis cases using a barycentric map over an n -simplex. Given the SDFs $\phi_{i,j,k}^i$ for each geometry $i \in \{1, \dots, n\}$, the interpolated SDF $\bar{\phi}_{i,j,k}(d)$ is computed as a weighted sum of the individual SDFs:

$$\bar{\phi}_{i,j,k}(d) = \sum_{i=1}^n w_i \phi_{i,j,k}^i(d),$$

subject to the constraints

$$\sum_{i=1}^n w_i = 1,$$

and

$$w_i \geq 0 \quad \forall i \in \{1, \dots, n\}.$$

Here, the weights w_i are the barycentric coordinates corresponding to the location d within the n -simplex defined by the n input geometries. The resulting interpolated SDF $\bar{\phi}_{i,j,k}(d)$ provides a continuous scalar field that represents an interpolation of the original geometries within the simplex. Though the actual parameter space is high-dimensional, involving the morphing of a complex, three-dimensional surface, we are able to effectively parameterize this using the dimension of the simplex n .

2.3 Geometry reconstruction

After computing the interpolated SDF $\bar{\phi}_{i,j,k}(d)$ using the barycentric weights, the interface of the interpolated geometry is extracted. The interface corresponds to the numerical zero-level set of $\bar{\phi}_{i,j,k}(d)$, identified by:

$$\Gamma_{i,j,k} = \begin{cases} 1 & \text{if } -\epsilon \leq \bar{\phi}_{i,j,k}(d) \leq \epsilon, \\ 0 & \text{otherwise,} \end{cases}$$

where ϵ is a small positive threshold that depends on the scale of the models. In our testing we found that while this value had to be hand-tuned, it was relatively insensitive across the dataset.

Finally, we reconstruct the surface geometry of the interpolated object. This is achieved by applying the marching cubes algorithm [16] to the binary scalar field derived from $\Gamma_{i,j,k}$. The marching cubes algorithm generates a triangulated mesh that approximates the surface $\partial\Omega$, where Ω is the region inside the geometry corresponding to $\Gamma_{i,j,k} = 1$. The vertices \mathbf{v}_m and faces \mathbf{f}_n of the resulting mesh \mathcal{M} are constructed by interpolating the positions within the voxels where the interface $\Gamma_{i,j,k}$ intersects the grid. The mesh \mathcal{M} , representing the reconstructed geometry, can be expressed as:

$$\mathcal{M} = \{\mathbf{v}_m, \mathbf{f}_n\} \quad \text{with} \quad \mathbf{v}_m \in \partial\Omega, \quad \mathbf{f}_n \subset \partial\Omega.$$

Here, \mathbf{v}_m are the vertices positioned on the surface $\partial\Omega$ of the interpolated geometry, and \mathbf{f}_n are the faces connecting these vertices to form a closed surface. To refine the mesh and remove artifacts like sharp corners resulting from the marching cubes algorithm, an iterative Laplacian smoothing operation [24] is applied, where each vertex \mathbf{v}_m is adjusted based on the average position of its neighboring vertices $\mathbf{v}_m^{(i)}$:

$$\mathbf{v}'_m = \mathbf{v}_m + \lambda \sum_i (\mathbf{v}_m^{(i)} - \mathbf{v}_m),$$

where \mathbf{v}'_m is the new position of the vertex after smoothing, and λ is a smoothing factor. It is evident that with an increased ray-tracing resolution, the reconstruction more closely approximates the fidelity of \mathcal{T} .

We have developed a software package that uses the above methodology to generate arbitrary-sized datasets. It is available to use on Github: <https://github.com/benjamark/didymus/>. The ray-tracing has been GPU-accelerated and tested on up to 10 billion rays, which provides reconstruction at a sufficient resolution for reconstruction of a realistic automotive model.

2.4 Properties of the interpolated SDFs

The use of the SDFs $\phi_{i,j,k}(d)$ for the interpolation provides advantages for the generating shapes from which a robust reconstruction can be made. The properties that make this possible are enumerated below:

- **Continuity:** The interpolated SDF $\bar{\phi}_{i,j,k}(d)$ is a convex combination of the basis SDFs $\phi_{i,j,k}^i(d)$. Given that each $\phi_{i,j,k}^i(d)$ is discretely continuous, $\bar{\phi}_{i,j,k}(d)$ is also continuous. The continuity argument guarantees that for any level (c), the level set ($\{x : \phi_{i,j,i}(x) = c\}$) will vary continuously as (k) changes. The zero level set is not guaranteed to exist, but it is *likely* to exist when the basis SDFs have sufficient intersection, and are not completely disjoint, which is something that can be ensured when positioning the basis STLs.
- **Feature Preservation:** $\bar{\phi}_{i,j,k}(d)$ will not introduce new geometric or topological features that were not present in the basis SDFs $\phi_{i,j,k}^i(d)$. Since the interpolation is a convex operation, no new critical points or disconnected components are generated. For example, interpolating between two similar car SDFs will not introduce a hole or an additional disconnected surface. The zero-level set $\{x : \bar{\phi}_{i,j,i}(x) = 0\}$ will reflect the features of the original zero-level sets.
- **Inclusion:** If one basis SDF $\phi_{i,j,k}^A(d)$ is fully contained within another $\phi_{i,j,k}^B(d)$, then the interpolated SDF $\bar{\phi}_{i,j,k}(d)$ will also be contained within $\phi_{i,j,k}^B(d)$ for all $k \in [0, 1]$. This inclusion property ensures that if one shape is nested inside another in the original SDFs, the interpolated shape remains within the boundary of the outer shape. For example, if $\phi_{i,j,k}^A(d)$ is the SDF of a sedan, and $\phi_{i,j,k}^B(d)$ is its estate equivalent, such that the rear roofline of the sedan is fully contained within that of the estates, the interpolation will produce shapes contained within the surface of the estate.

3 Simulation and data-driven model design

3.1 Geometry and dataset

To best represent the complexities of a realistic automobile, we consider the DrivAer model [13], an open-source midsize passenger car geometry (Figure 2), developed to assess the quality of and contrast automotive aerodynamics investigations carried out using computational fluid dynamics tools [2]. The model is available in three configurations: a fastback, estate, and sedan, shown in Figure 3. Elrefaie *et al.* [8] used this geometry as a starting point, but only considered discrete, parameteric modifications, and predicted the scalar drag coefficient using a point cloud representation.

While their dataset provides a high quality set of realistic geometries, we construct a dataset organically by interpolating between the three DrivAer configurations to generate a family of designs, our only parameters being the choice of basis designs to interpolate between. The three configurations are different enough so as to provide a sufficient variation in drag coefficient (the separation aft of the vehicle being significantly



Figure 2: Perspective view of the DrivAer geometry in notchback configuration

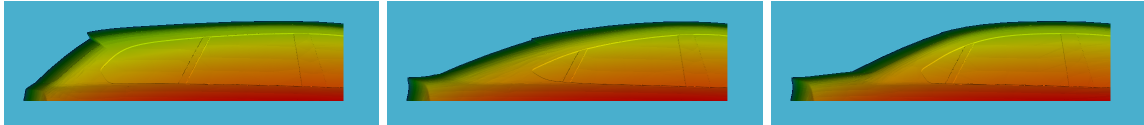


Figure 3: DrivAer back configurations: estateback (left), fastback (center) and notchback (right).

impacted by the form of the rear roof slope), but also similar enough to provide a controlled testing ground for our proposed methodology.

As a test of the ray-tracing approach, we present an example of reconstructing the notchback model using a ray-tracing resolution of 1024^3 rays in Figure 4. We see that the reconstruction faithfully captures the surface features of the original, and the new mesh is watertight, which makes generating the CFD mesh simple. We notice that there is a faint, spurious, low-amplitude rippling in certain regions of low curvature and detail, which is an artifact of the finite resolution of the ray-tracing. These attenuate with increasing resolution, just as errors in the STL representation of the underlying CAD curves attenuate with a finer triangulation. We will show in our discussion that follows that these ripples do not have a significant impact on the flow solution.

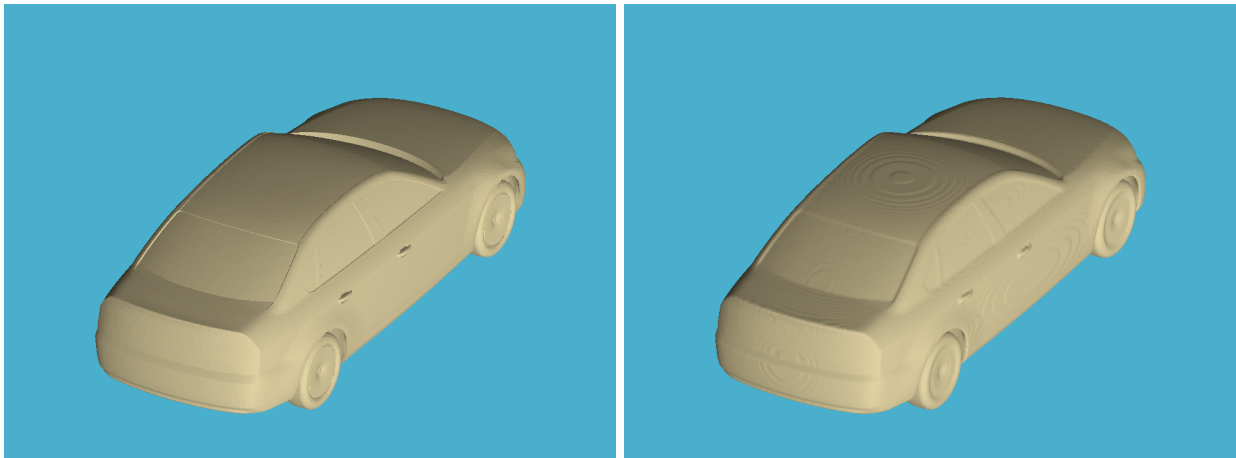
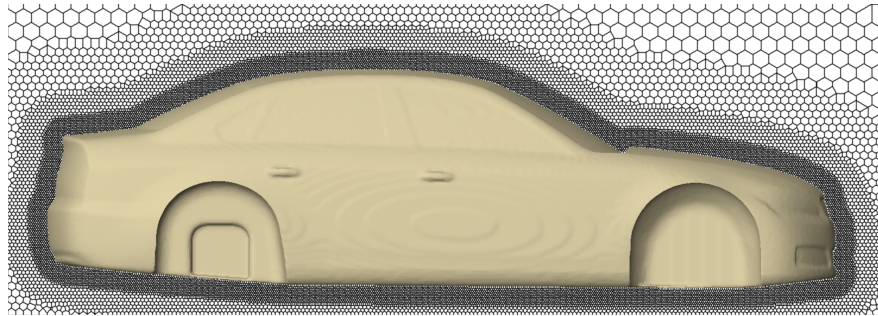


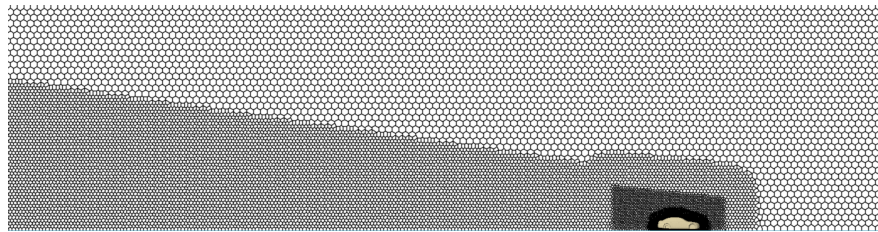
Figure 4: Left: Original STL; right: reconstructed STL.

3.2 Large-eddy simulations

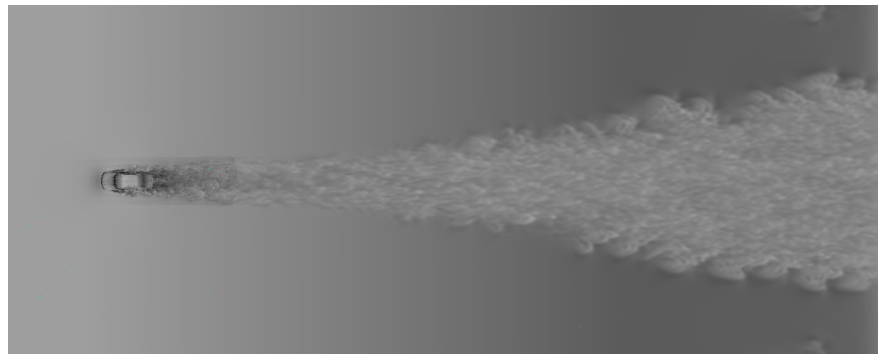
To generate the training dataset for the neural network, large-eddy simulations (LES) of the airflow past the DrivAer geometry at 85 mph with no wheel rotation are performed using the low-dissipation CharLES solver. Details of the Voronoi diagram-based meshing paradigm used in the tool can be found in Brès *et al.* [5], and the formulation of the low-Mach Helmholtz pressure solver is outlined in Ambo *et al.* [1]. The



(a)



(b)



(c)

Figure 5: View of the mesh used for the large-eddy simulations, with refinement zones shown: (a) near the car, (b) in the wake. (c) Instantaneous velocity magnitude contours showing wake behind the car.

code has been validated in aerodynamics analysis of a number of high-Reynolds number flow studies [10]. The mesh uses 2 million control volumes, with refinement near the no-slip surfaces of the car, as shown in Figure 5. The resolution on the car surfaces is $\Delta/L = 0.0023$, where Δ is the mesh size there, and L is the characteristic length of the car. The domain is sized at $32L \times 5L \times 5L$, with the car placed at $8L$ from the inlet. Since the Helmholtz formulation permits low-frequency pressure oscillations, we use a numerical sponge at $2L$ from the domain boundaries to reduce the time for the reflecting waves to be damped out. The Vreman subgrid model is used to approximate the effects of the subgrid scales on the resolved scales, and walls are modeled using the algebraic wall model. The flow is initialized with a converged initial condition from the baseline DrivAer notchback geometry. The simulation is run for a total time of two seconds, and statistics are collected for the last one second. Figure 6 shows the instantaneous drag coefficient, computed as follows:

$$C_d = \frac{2F_d}{\rho v^2 A}$$

where F_d is the drag force, ρ is the fluid density, v is the freestream flow velocity, and A is the frontal area of the car projected in the direction of the flow. The initial spike is from the recalibration of the flow to the new boundary conditions (the new geometry), and the averaging begins well after equilibrium has been established.

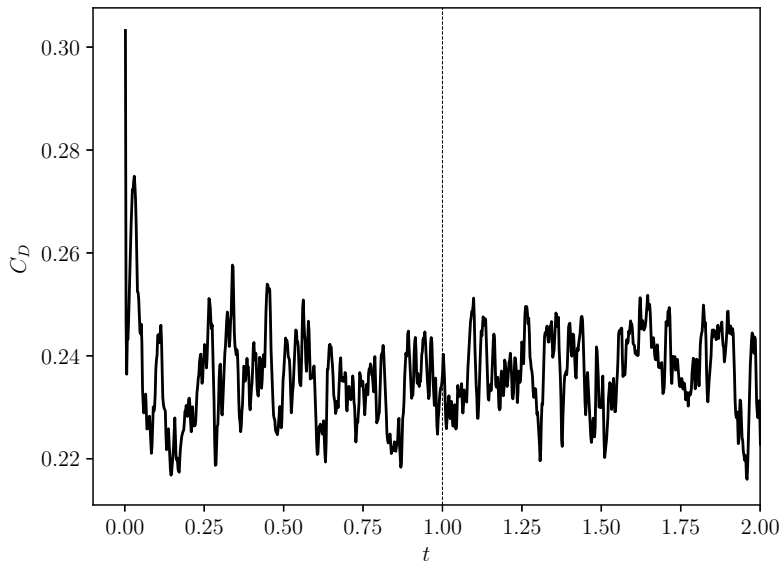


Figure 6: Time history of drag coefficient for a single geometry. The dashed line indicates the start of the averaging window. The geometry and boundary conditions are to scale, so the time scaling is true to real-world time.

The wall time for a single simulation to run to convergence is about 12 minutes on an NVIDIA H100 GPU [7]. A sample flow visualization depicting the velocity magnitude projected on to the floor of the domain is shown in Figure 5, showing that the entire width of the wake is encapsulated in the domain. As mentioned above, care is taken to ensure that the mesh resolution at the wall is comparable to the length scale introduced by the ray-tracing, which are $\sim L/1000$, where L is the length of the car, in order to ensure that discretization effects are consistent across different stages of the workflow. The simulation setup and parameters largely follow our previous work on the same flow [3]. The effects of the ray-tracing are most evident in the reconstruction in regions of low but non-zero surface curvature, and manifest themselves as low-magnitude ripples, such as in the door panels in Figure 5 (a).

3.3 Network I/O

The choice of representation of the geometry is made evident when one considers that drag depends not on the internal design of the car, but only the wetted surface, which scales as $\mathcal{O}(N^2)$ on a $\mathcal{O}(N^3)$ volume, where N is the characteristic number of points along one dimension of a discretized representation of the geometry. Thus, projections of the exterior surface are a natural representation choice for the geometry. For instance, Song et al. [23] developed a surrogate model that used isometric views of automobile designs from the ShapeNet database [6]. Projections can be naturally assembled into structured image data that can be processed by convolutional neural networks (CNNs) [18]. CNNs are the most popular neural network architecture of choice for image processing, owing to the shared-weight model of the neurons, allowing for the same feature, say, an edge or sharp corner in an image, to be learnt across the whole image by the same kernel. Fewer connections across a single layer of a network leads to a smaller network that is less prone to overfitting. CNNs are also advantageous from an ease-of-training standpoint relative to graph networks or point clouds [8], the architecture of choice for unstructured representations. A graph representation of a geometry is also highly sensitive to small changes, and not an ideal way to represent a surface mesh, where the connections between two nodes do not have the same significance as in an actual graph network; i.e. there can be several valid tessellations of the same geometry. Our inputs to the model are three planar projects of the geometry: the back, the side, and the top (shown in Figure 7), stacked to make three channels. We note here that the this choice is prompted by the fact that the geometries are identical in the other views, either due to symmetry, or the fact that the variation is restricted to the rear roofline. In general, we could use all six views (the current three, and the left side, bottom, and front views) to get maximum coverage. Each pixel records the shortest distance from the plane of the camera to the point on the vehicle. The image resolution is 384×384 , which is chosen to match the resolution of the mesh cells of the CFD and the resolution of the ray-tracing. This choice is done in keeping with the need to resolve sufficiently fine changes to the surface. Concretely, taking the different discretization choices (ray-tracing, mesh, and image resolution) into account, we expect to detect a change of about 12 millimeters to a surface in a vehicle that is 4 meters long. The data in the images is binned into 255 bits.



Figure 7: Inputs to networks; left: back view, center: side view, right: top view.

While the drag coefficient is a useful average measure, design is driven by spatial information of pressure. We thus train networks to predict quantities of interest at three levels of abstraction: the scalar drag coefficient, the vector centerline surface pressure along the axis of symmetry of the model, and the full surface pressure information in the aforementioned three views. Individual neural networks are trained for each of these QOI. Figure 8 shows a selection of samples from the dataset. One can see how the roofline is gradually morphed to produce designs intermediate to the basis cases. It is also evident how regions of low pressure are more apparent in the more estate-like designs, which is a result of the larger separation bubble that that design tends to produce. With this method of generating training samples, the parameterization is not tied to discrete design features such as the door mirrors or handles [3], but a comprehensive three-dimensional morphological operation, designed to provide a high density of data point clustering in feature space.

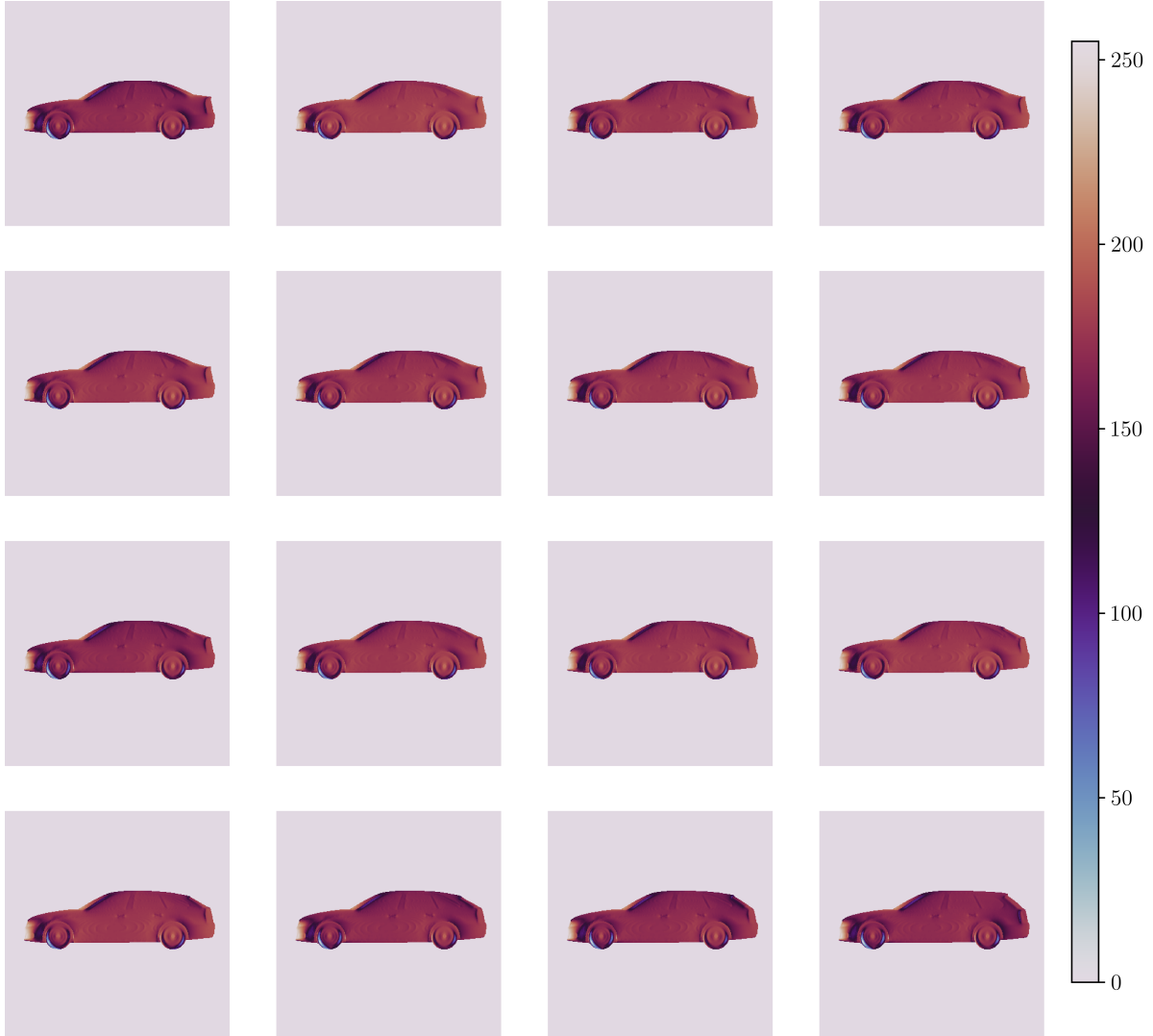


Figure 8: Normalized surface pressures shown on left side views of a selection of samples in dataset, showing a transition from the notchback (top left) to the estateback (bottom right), with the fastback visited along the way.

3.4 Dataset

The number of samples per dimension of the simplex is taken to be $n = 50$, which gives us $\frac{n(n+1)}{2} = 1275$ total geometries, for which we compute flow solutions as described above. Since the simplex in 3D is a triangle, it is convenient to plot each sample in a barycentric map, colored by its drag coefficient (Figure 9). This plot provides an intuitive overview of the entire database, and similarity of a given sample to a certain corner case is directly available as the Euclidean distance between their barycentric coordinates. As one expects, the fastback (right vertex) has the lowest drag, followed by the notchback (top) and finally the estate (left). We observe faint banding in the drag coefficient contours, along directions parallel to the sides of the triangle. This is from stair-stepped artifacts that stem from the finite resolution used in the ray-tracing, and reduces as the discretization error for the geometry is reduced.

Table 1: Simulation and dataset parameters

Mesh size	2M CVs	No. of basis cases	3
Wall model	Algebraic	No. of total samples	1275
Subgrid model	Vreman	Normalization	Min/max
Simulation time	2 s	Train/val split	1069/141

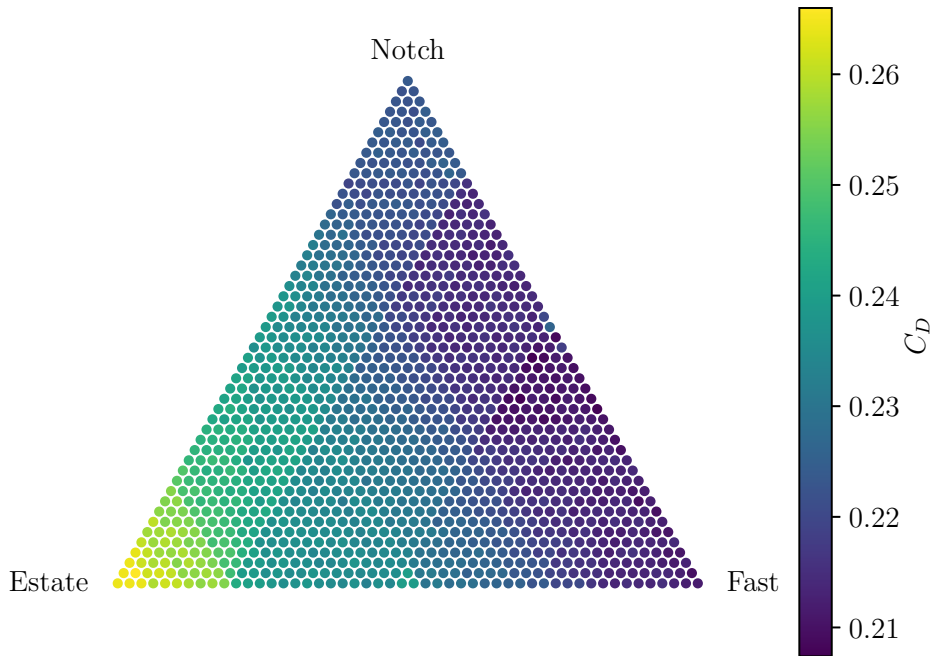


Figure 9: Barycentric map showing drag coefficient of dataset

3.5 Network architecture

The architecture of all the networks is convolutional. The three networks downsample the input of dimension $384 \times 384 \times 3$ down to a bottleneck of $24 \times 24 \times 256$ in the same way; however, the scalar network has an output of size 1, and the vector network 384, both after going through a fully-connected layer of size 24. For the tensor case, we use a U-Net architecture [20] with symmetric skip connections, as shown in Figure 10. The skip connections serve to greatly improve the recovery of localized information that may be lost in the several convolutional layers that the information passes through [28]. Maximum pooling layers are used after each convolutional layer to preserve and highlight important features. A summary of the model architecture is provided in Table 2. Since the inputs to all three models are the same images, we keep the same architecture for the contracting part of the network, since the feature encoding is expected to be similar. One may envision this as a form of transfer learning, where the scalar model is tuned, and the architecture of the convolutional layers is retained for the vector model, and subsequently for the tensor model. All layers, however, are trained from scratch in the three types of models. The hyperparameters for the network — the learning rate, the number of filters per layer, and the optimizer type — are tuned by a grid search. We perform aleatory and epistemic uncertainty quantification on the scalar and vector networks by the method of ensembles, and this is reported in an appendix.

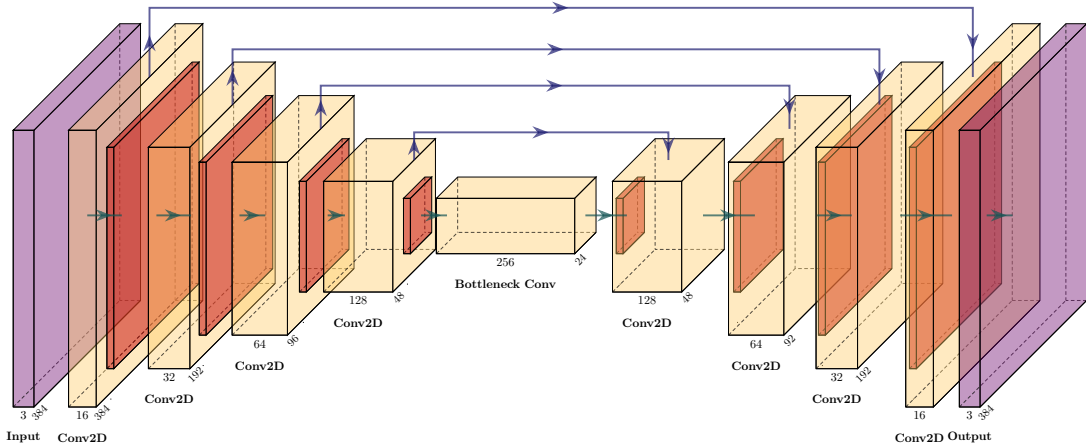


Figure 10: Schematic of U-Net architecture for the tensor model.

Table 2: Network architecture

Architecture	CNN/U-Net
Activations	ReLU
Pooling	Max
Loss	MSE
Epochs	500
Optimizer	Adam
Learning rate	10^{-3}
No. of parameters	50K (1D model), 250K (2D), 1M (3D)

4 Results and discussion

4.1 Scalar outputs

Figure 11 shows the performance of the model trained to predict the scalar drag coefficient on the test set consisting of 65 samples. The figure is rescaled by the lowest value of the ground truth, and shows a range of about 500 drag counts of variation, defined as

$$\Delta C_D = C_D \times 10^4$$

where C_D is the drag coefficient. The drag count simplifies comparisons across different configurations by scaling the drag coefficient to a more intuitive range. The measure is particularly useful when evaluating subtle changes in aerodynamic design. The network shows excellent predictive performance, with a 95% percentile accuracy of 24 counts. The controlled nature of the dataset also allows us to plot the error on the barycentric map (Figure 12), which gives us insight into the localization of the error. The quantity plotted is the relative error $\left| \frac{C_D^{\text{true}} - C_D^{\text{pred}}}{C_D^{\text{true}}} \right|$. While the current example does not show any error bias toward any of the three corners, it is evident that in cases where an initial equal sampling of data points in barycentric space produces an error response surface that contains regions of high error, a targeted resampling can be done, rather than a blind and expensive uniform increase in samples.

4.2 Vector outputs

We next consider the case of the vector output: the centerline surface pressure of the cars, extracted from the same input images. Figure 13 shows a heatmap of the model predictions on the entire test set, and a comparison with the ground truth shows that the performance is likewise excellent in this case. An overlay

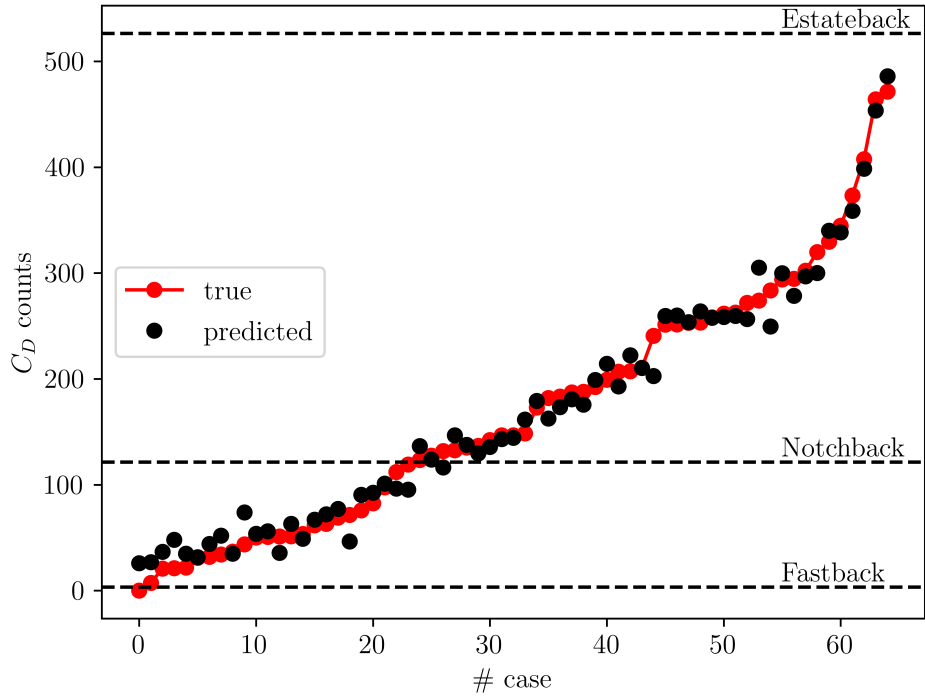


Figure 11: Scalar model performance on test set, organized by increasing value of the ground truth. Horizontal dashed lines represent the reference drag coefficient values of the basis geometries.

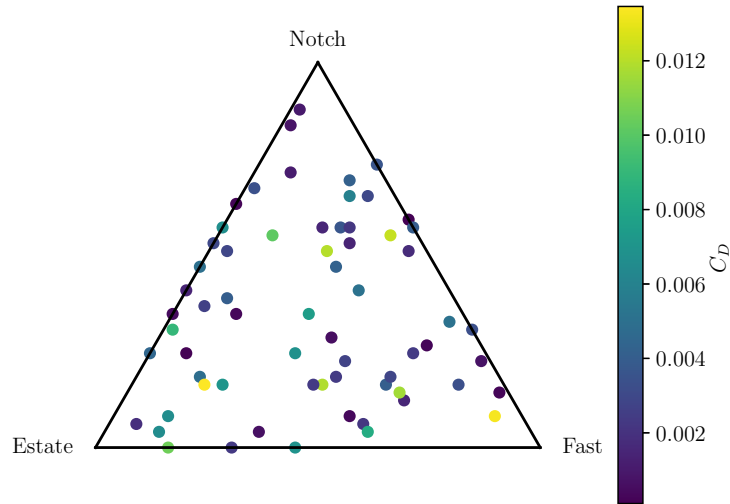


Figure 12: Scalar model error on test set.

plot of all the curves in the test is shown in Figure 14, which shows that the spread of values between pixel 50 and 150, which represents the zone of high geometric variance in the dataset corresponding to the back of the vehicle, is well captured.

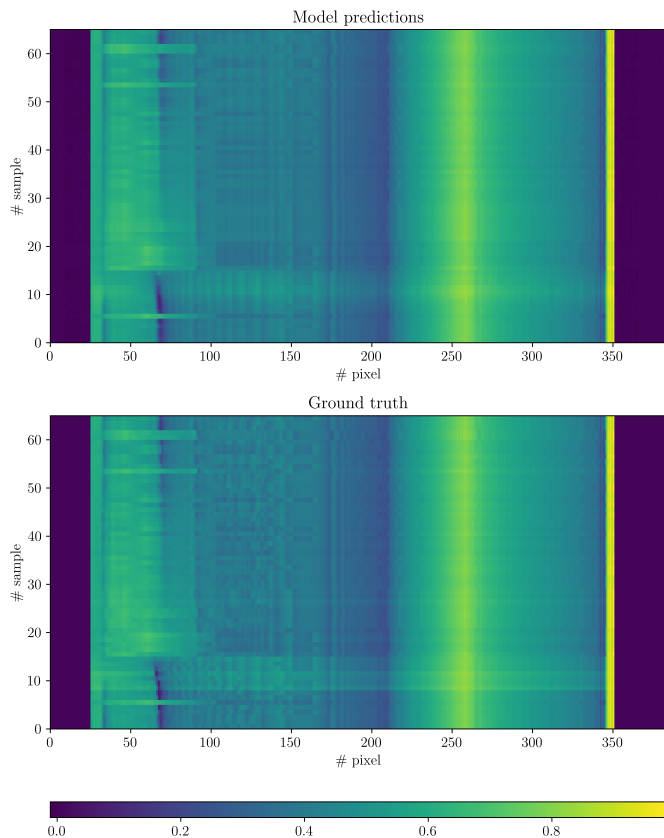


Figure 13: Heatmap of vector model performance on test set. The car is facing right.

4.3 Tensor outputs

Figure 15 shows the average error over the whole testing set of 65 samples for the three different channels. The reconstructions are of good quality, with precise capture of localized features owing to the skip connections, which preserve memory across the central constriction. We see the presence of some crosstalk between the three images, showing that the three channels are not perfectly disentangled in the training phase. However, the absolute magnitude of the error is low ($\mathcal{O}(10^{-3})$). Areas of high concentration of the error include the trunk hatch, which is the region where the flow separates and the impact of the recirculation bubble on the surface pressure is seen, and the wheel arches. The mean and standard deviation of the error over the whole test set is shown in Figure 16; we see consistent performance across all samples, with a tracking of the two quantities.

We next examine the performance of the networks for a single test set sample at all three levels of output abstraction. Figure 17 shows the scalar QOI; Figure 18 shows the vector QOI. In both cases we see good agreement with the ground truth; we see in the vector case that the only significant discrepancy comes from an underprediction of the surface pressure between pixels 100 and 150, which is the region just aft of the C-pillar of the car that lies within the separation zone. Figure 19 shows that the tensor case is also reconstructed with good quality,

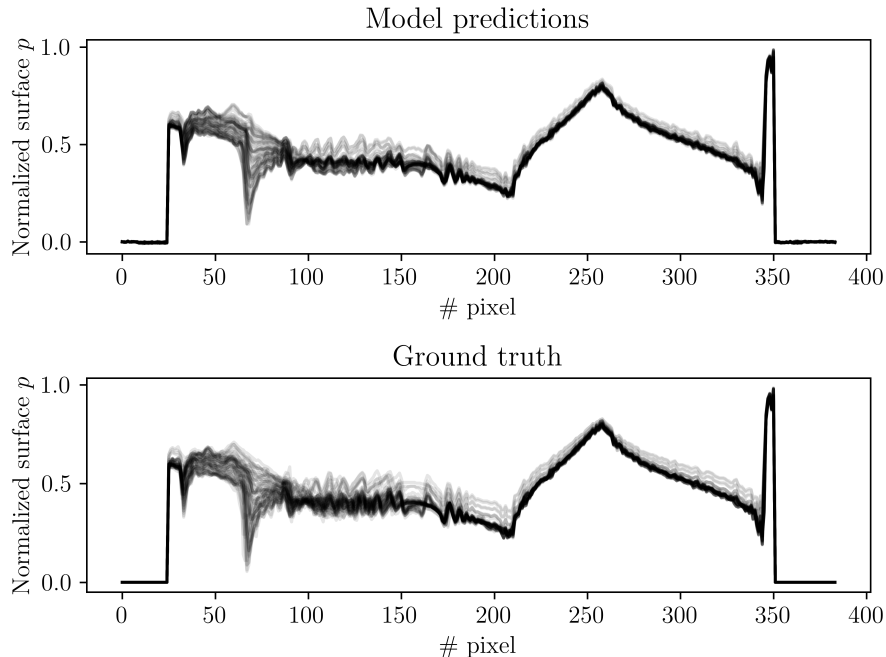


Figure 14: Vector model performance on test set. The car is facing right.

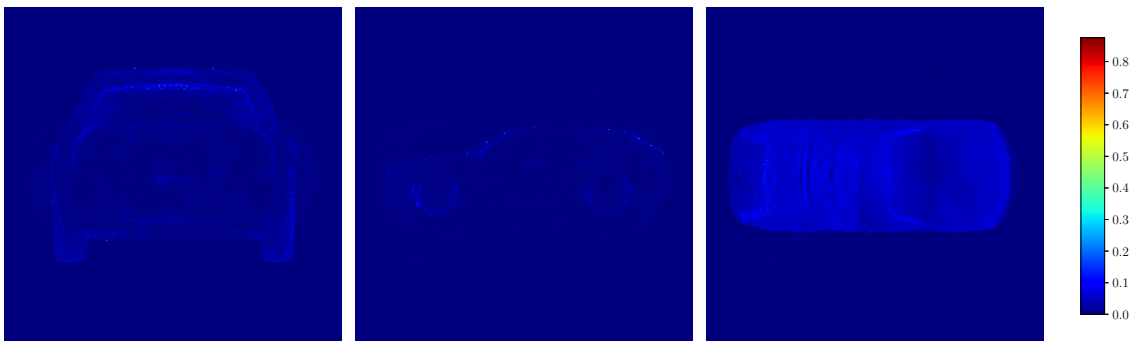


Figure 15: Mean absolute error (MAE) of normalized surface pressure over whole testing set. Left: channel 1, center: channel 2, right: channel 3.

4.4 Network extrapolation

The benefit of using a controlled dataset is the increased granularity it can provide from the high-density of samples in the input feature space. This attribute also encourages one to consider the possibility of extrapolation to unseen data. To do this also in a curated manner, we consider the incircle of the barycentric map, and construct a training set of points inside it (see Figure 20). Then, we test the model on samples outside the incircle. This is not entirely undirected extrapolation, since all samples in the triangle — barring points on the edges — are made up of a linear combination of the three basis; nevertheless, this is a case where the training and testing distributions undoubtedly differ. Moreover, we have a clear visual understanding of which samples in the test set are expected to be more difficult to predict, simply by considering the distance from the corners (see Figure 20 (right)).

Figure 21 shows the results of these investigations. We see that the model does a remarkable job of predicting trends in the drag in the extrapolated region. However, there is error incurred in the most non-

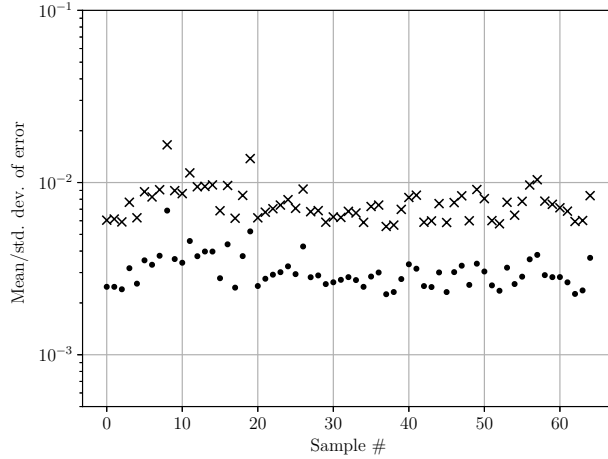


Figure 16: MAE of test set. Mean (dots) and standard deviation (crosses).

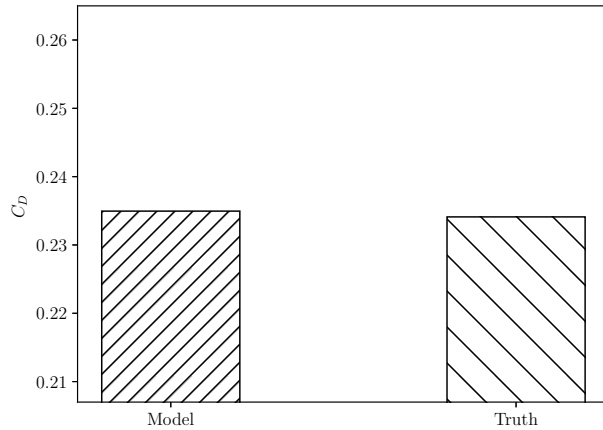


Figure 17: Comparison of scalar level error for one test set sample.

linear portion of the map, the corner with the estateback, as seen in Figure 22. As we expect, the error grows with distance orthogonally away from the incircle, from the basic accuracy of about 25 to 50 counts, to about 150 counts.

4.5 Effect of uniform barycentric sampling

To demonstrate the impact that a controlled sampling has on prediction quality, we examine a subset of 36 training samples, and train two models: in the first, the points are sampled uniformly in barycentric space. In other words, the samples per dimension is 8, which gives a triangle number of 36. In the second model, the points are sampled randomly in barycentric space, to simulate an uncontrolled dataset. In this case, we test an ensemble of models with different random seeds and report a model with representative results. The models are trained to predict the scalar drag coefficient. The results from this experiment are shown in Figure 23, on the same 65 test set samples from earlier experiments. We see that the effect of the controlled sampling is to produce a network with a high quality of predictions: the 95% percentile accuracy is 51 drag counts. The uniform sampling produces a network with insufficient coverage of the different portions of the

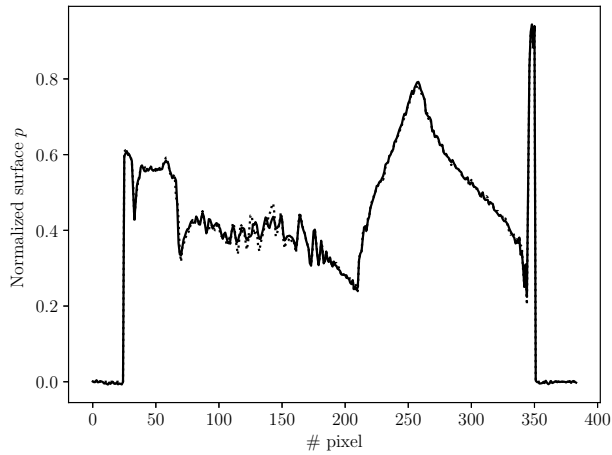


Figure 18: Comparison of vector level error for one test set sample. Solid line: model predictions; dashed line: ground truth.

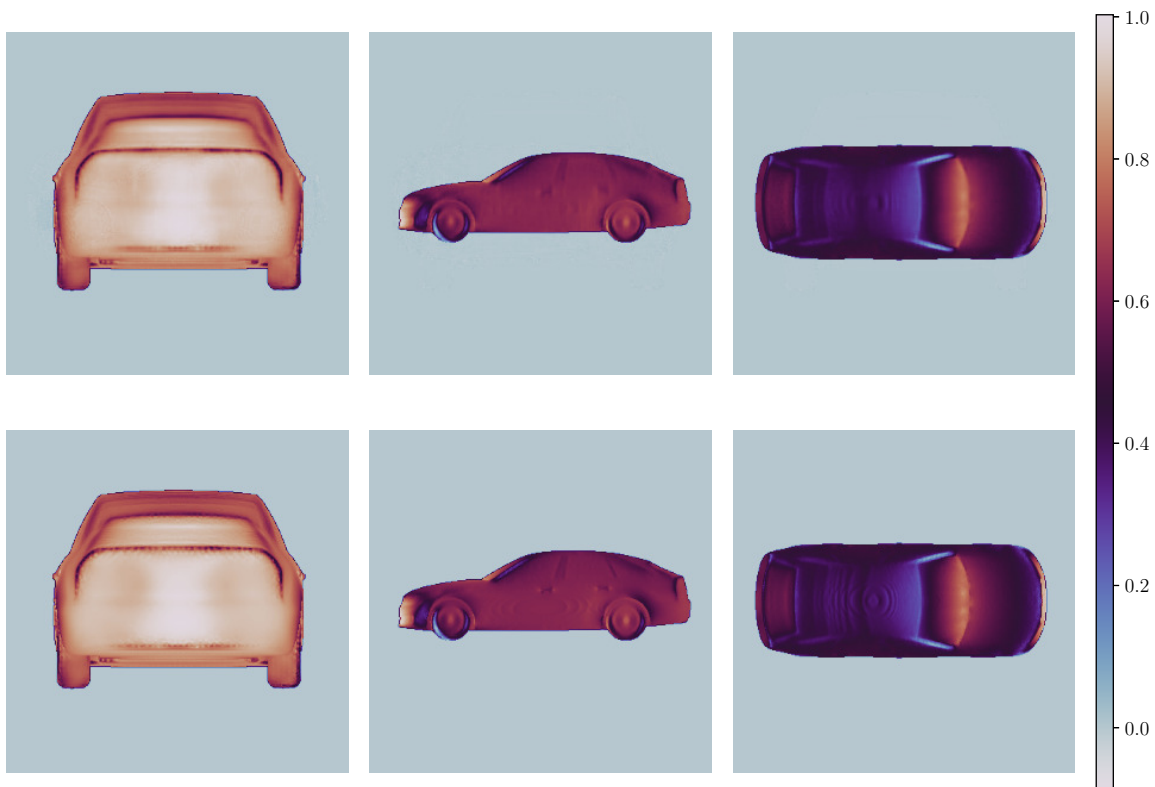


Figure 19: Comparison of tensor level error for one test set sample. Top row: model predictions; bottom row: ground truth.

simplex, and has a much lower accuracy of 108 counts. This shows that even with a complex and non-linear response function, using equispaced training points enables better performance.

To understand the difference in performance, we investigate the loss landscape of the two models, by

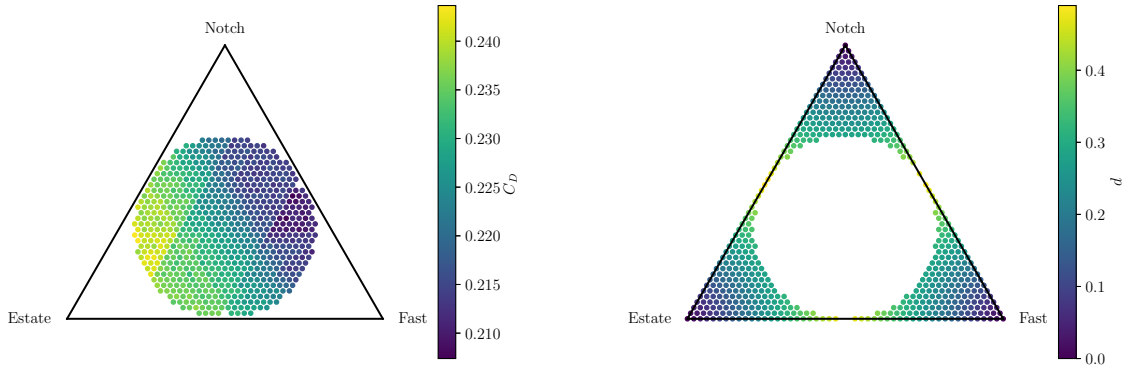


Figure 20: Training set C_D for extrapolation (left) and test set distance from corners (right).

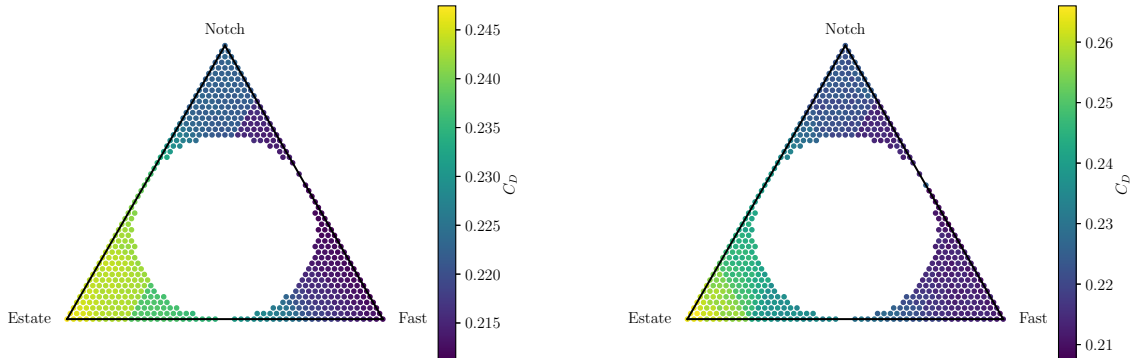


Figure 21: Model predictions (left) and ground truth (right) for scalar extrapolation test.

perturbing the network weights. We apply perturbations to the weights of different magnitudes, and compute the corresponding change in loss function. This allows us to visualize the stability and generalization potential of the networks. The maximum perturbation strength — 0.01 — is chosen to give an intermediate-scale picture of the loss landscape, between the overall shape, and the finest details. The loss landscapes for both the uniformly sampled and randomly sampled models are shown in Figure 24. The analysis reveals that the uniform sampling results in a loss landscape with greater fluctuations, indicative of sharper minima and potentially less robust generalization. In contrast, the non-uniformly sampled model displays a smoother landscape, suggesting a broader and more stable basin of minima, thereby indicating better generalization potential.

4.6 Comparison with other models: Gaussian Process Regression

The excellent results obtained by the CNN on the generated dataset prompt us to investigate the non-linearity of the problem: i.e. is the prediction of aerodynamic drag on this dataset possible with a much simpler model? This question is best answered in an *a posteriori* setting, by comparing the performance of the CNN in the scalar case (the simplest) with another non-linear model. We avoid the obvious linear model (least-squares regression) because it is evident from Figure 9 that the variation in drag coefficient over the barycentric map is non-linear. The most suitable reference for these investigations, therefore, is Gaussian Process Regression (GPR). GPR is a non-parametric, Bayesian inference model that offers a flexible approach

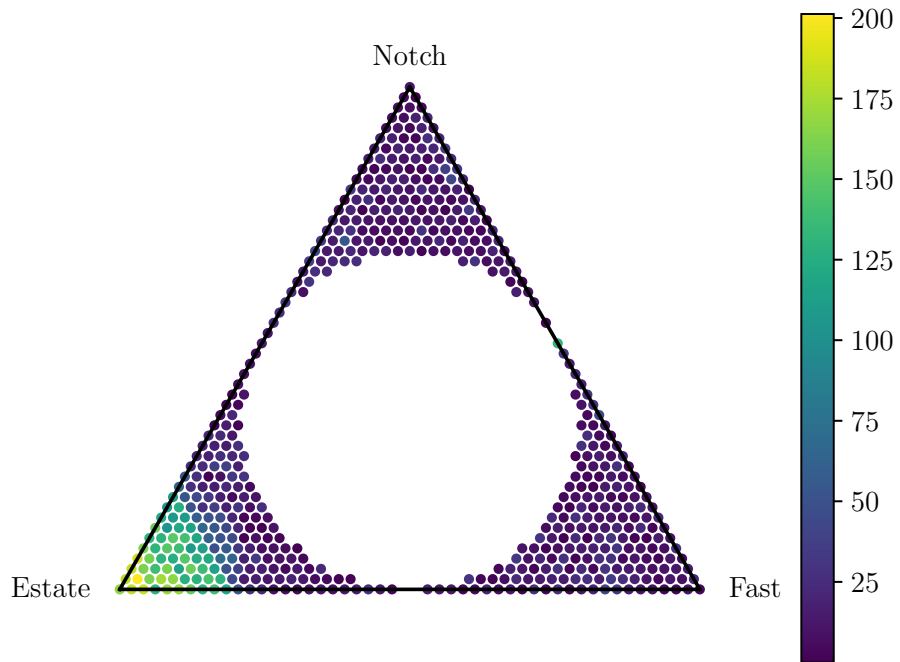


Figure 22: Mean absolute error for model predictions in scalar extrapolation test.

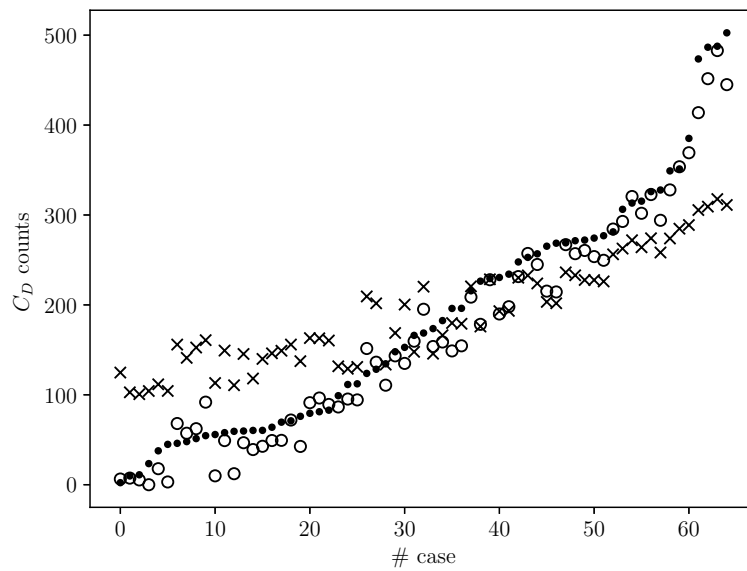


Figure 23: Scalar model performance with reduced dataset sizes; dots: ground truth; circles: uniform barycentric sampling; crosses: random barycentric sampling.

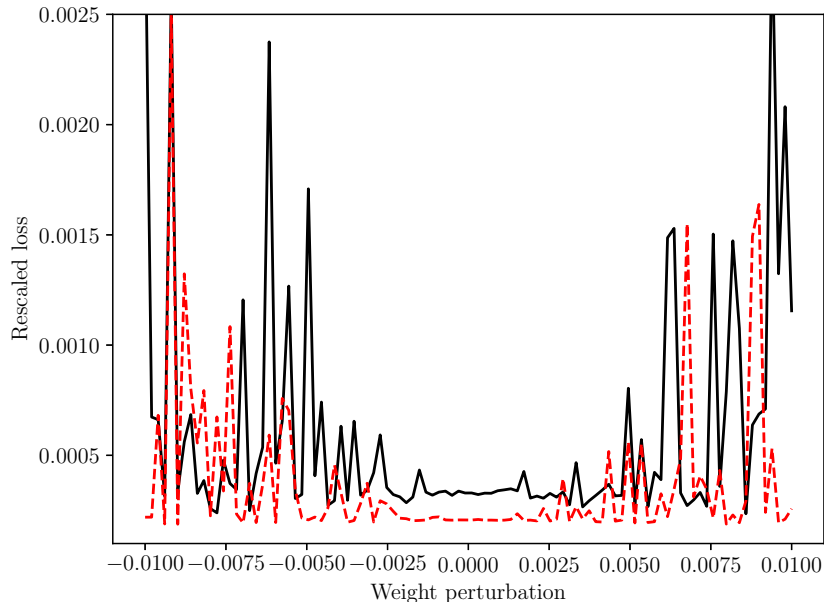


Figure 24: Loss landscape comparison for scalar models; dashed red line: uniform barycentric sampling; solid black line: random barycentric sampling. The curves have their means subtracted out to better emphasize fluctuations.

to regression by defining a distribution over functions [27]. Since the purpose of this exercise is to investigate the complexity of the dataset, we directly feed the model the barycentric coordinates (x, y) that correspond to the geometries. This is another benefit to the database generation procedure we have outlined: each data point is identifiable uniquely by its position in the simplex.

The covariance function (or kernel) plays a critical role in the performance of GPR. We use a composite kernel $k(x_i, x_j) = \sigma_f^2 \exp(-\frac{1}{2\ell^2} \|x_i - x_j\|^2)$, where $\ell = 1.2$ is the length scale and $\sigma_f^2 = 1.0$ is the signal variance. The model was optimized by using the maximum likelihood framework for hyperparameter tuning, with 10 restarts and a noise term $\alpha = 10^{-10}$. We observe from Figure 25 that the tuned GPR model, while predicting the test set with fairly good accuracy (R^2 score 0.92), still struggles to match the performance of the CNNs. While the 95th percentile accuracy for the CNNs was 24 drag counts, it is 58 for the GPR. We reiterate that the variation of C_D across the three designs is primarily due to the separation from the roofline, which varies in a complex, three-dimensional way across the dataset. Thus, GPR requires an even higher sampling than the 50 points per dimension we have used in this case. Since GPR models the prediction as a distribution, one can directly obtain uncertainty quantification bounds from the standard deviation of each output. This is also plotted in Figure 25. A comparison with ensemble uncertainty quantification of the CNNs is shown in an appendix, and one observes that the confidence intervals for GPR are much broader for the same dataset.

5 Conclusions

In this work, we address the problem of availability of high-quality geometries for training data-driven models for aerodynamics analysis. Focusing on automotive drag prediction, we develop a method by which an arbitrary database of high-quality, realistic models can be systematically generated from a small number of starting designs. Our workflow involves the conversion of the STL representation of the geometry to an intermediate binary representation using an open-source ray-tracing tool we have developed, followed by barycentric interpolation to generate new designs. The method has been tested using the three starting configurations of the DrivAer model, and we show that the performance on quantities of interest of various complexity — scalar, vector and tensor — is excellent. Care has been taken to ensure that we are predicting

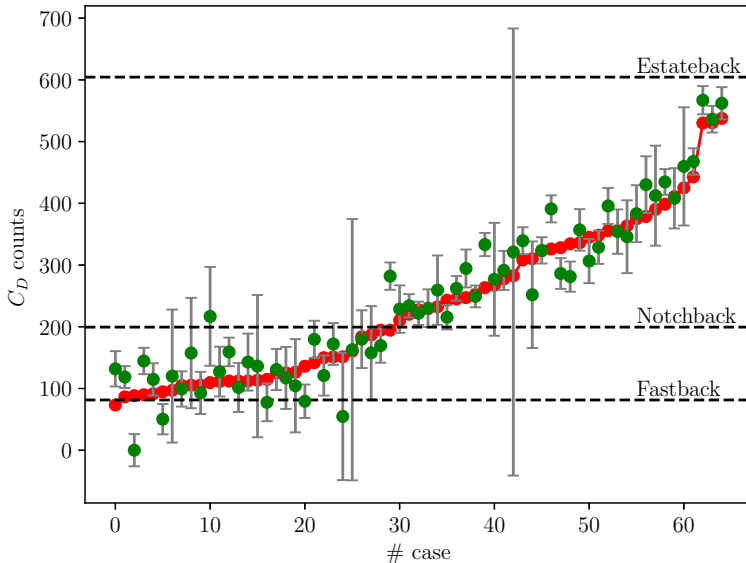


Figure 25: Performance over test set. Red dots: ground truth; green dots: results from Gaussian Process Regression. The y -axis is zeroed using the minimum value of the GPR predictions. Error bars represent 95% confidence intervals.

variations in morphology on a sufficiently fine level, in keeping with practical considerations for automotive design. We attribute the performance of our models to the granularity of the dataset, which allows the networks to learn a smoother representation of the drag than would be possible with an unstructured dataset made up of an assortment of geometries. To show this, we conduct *a posteriori* analysis of two networks trained on uniform and non-uniform barycentric sampling of the data respectively, and show that the former has a smoother loss landscape, leading to more robust generalization and predictive accuracy. We believe this method could be the basis for a universal drag predictor, given enough training samples in a sufficiently high-dimensional space. Ongoing investigations are centered around designing a dataset that could potentially work with all cars of a certain type, for e.g., sedans, and the task is to then identify what makes a suitable corner geometry. It is of course evident that if two completely incompatible shapes are chosen for the corners, interpolation between them would result in shapes not likely to be used in practical design; however, the key is that the network learns about the surface pressure on these shapes regardless of whether or not the intermediate designs are practical. Other work in the field has used transfer learning to good effect; Song *et al.* [23], for instance, use a pre-trained ResNet for their investigations, with only a few trainable layers at the end. It is possible that as the databases grow in size, the training process could benefit from a network that has had a broad exposure to a variety of inputs and can recognize fundamental image building blocks already. We are also interested in exploring other representations for the geometry. Images and CNNs have the benefit of ease of training, but suffer from the issue of occlusion in non-convex geometries (which includes most automotive shapes), so alternative representation approaches such as FNOs [14], which have been used in conjunction with graph representations of geometries [15], could be used. Our present workflow for generating geometries is easily compatible with any of these existing approaches. Another important piece of the problem is as follows: given a new, unseen geometry, what is the likelihood that the network prediction is within the expected accuracy based on the test set? In other words, how can we know that a given sample is out-of-distribution (OOD)? A solution for this might be to use convolutional autoencoders to use the same images we have used for the CNNs, to learn an encoding of the geometries in the dataset. Autoencoders used in this way have been successfully used to encode geometries in a parameter-free way [21]. This encoding — called a latent space representation — could then be used to determine whether or not a new geometry is OOD, and what the accuracy expected of the network can be. This ties in well with

the present planar projection representations of the present work, which work naturally with convolutional autoencoder, and will be an avenue for future investigations.

6 Appendix

6.1 Dataset ablation

To get a sense of the amount of data required for this problem, we perform ablation studies for all three models. The training set is gradually reduced in size, keeping the validation and test sets fixed. The network architecture is left unchanged. The results in terms of average MSE over all the test set are shown in Figure 26.

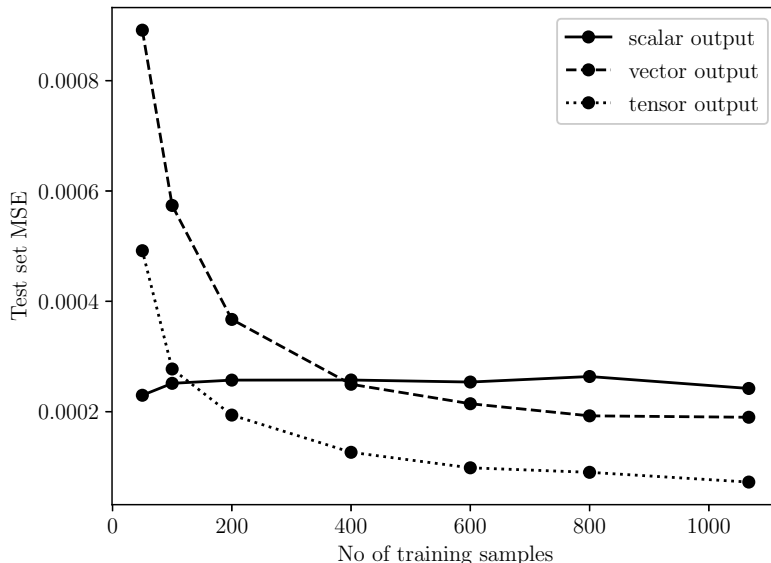


Figure 26: MSE as a function of training set size.

The models converge at all three levels of abstraction for approximately 200 samples, which corresponds to 20 samples per dimension. Below this, the tensor model degrades first, followed by the vector model, as expected. It is important to be sparse with the sampling in each dimension; with additional corner cases the simplex becomes higher dimensional and one is quickly confronted with the curse of dimensionality when ensuring sufficient coverage.

6.2 Uncertainty quantification

To establish confidence in the predictions of the model, we investigate various sources of uncertainty, focusing on both scalar and vector cases. The method we follow is one of ensembles of models [12]. We consider the following two types of input uncertainties:

- *Aleatory uncertainty*: Associated with the randomness in the learning process, this is not controllable. We consider two sources: the randomness of the initialization of weights in the model, which can have a significant impact on the converged optimum, and the selection of the batches used for training. The batch size is fixed at 64 after a hyperparameter tuning process, but there is still randomness associated with the elements in each batch, which affects the gradient computed at each step, and consequently the optimum.

- *Epistemic uncertainty*: This source of uncertainty is due to assumptions made in the model, and here we consider the choices made in the model architecture. We are interested in the impact that a perturbation to the size of the network can have, so we consider variations in the number of convolutional layers. Another important source of uncertainty is the impact that adding dropout layers can have, since this indicates how perturbations to the different connections in the network can impact the predictions. We note that the amount of dropout that is generally needed is much lower in convolutional networks (as opposed to fully-connected ones), owing to the need for the identification of local features, and the fact that connections are sparser to begin with.

Table 3 summarizes the variation in the ensemble of models. We follow the recommendations of Saetta *et al.* [22] in sizing the ensemble; they found that for a problem of similar scope, an ensemble size of 50 was sufficient to converge the uncertainty bounds. In the present work, we use 90 samples to build the ensemble.

Table 3: Details of UQ ensembles

Parameter	Uncertainty type	Range
Weights initialization	Aleatory	n/a (seed)
Batch selection	Aleatory	n/a (seed)
Number of Conv layers	Epistemic	3 to 5
Dropout %	Epistemic	0.5 to 2

Figure 27 shows the 100% confidence intervals of the models for all points in the testing set. We observe that there is a scatter of about 30 counts across the set (95th percentile), which is consistent with the accuracy of a single model with respect to the ground truth values. We also perform this ensemble analysis for the vector case (Figure 28), and see that there is an increased scatter near the back of the car between pixels 50 and 150, as we expect.

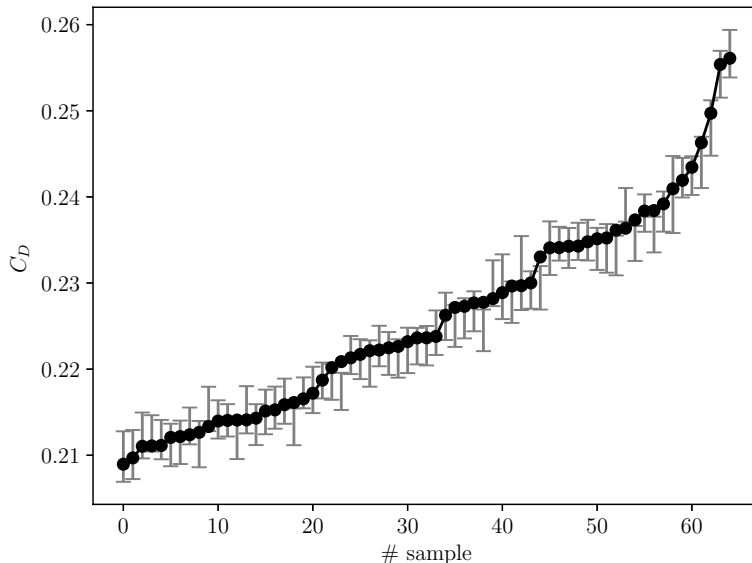


Figure 27: Scalar model 100% CI on test set. Black dots represent ground truth values.

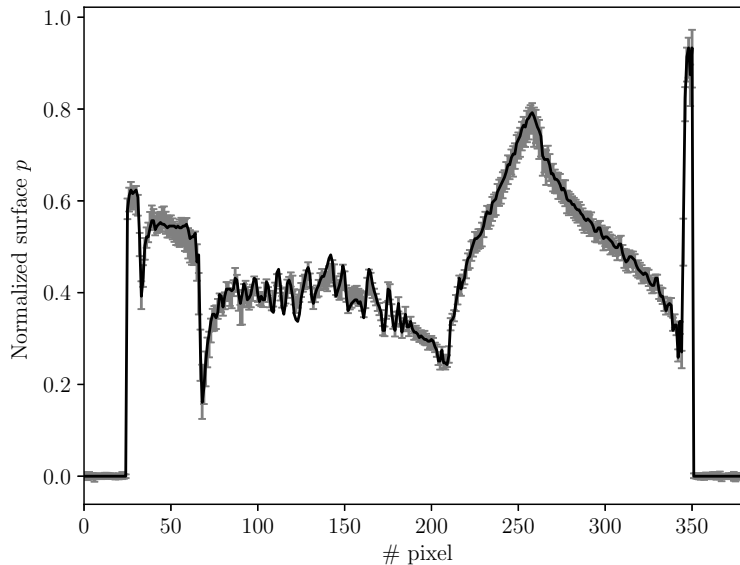


Figure 28: Scalar model 100% CI on test set. Black line represents ground truth values.

Data availability statement

All data used in this study will be made available upon request. The software developed in this work is released as an open-source project on Github.

Acknowledgments

Computations performed in this work were performed on the Kestrel Computing System at the National Renewable Energy Lab, Golden, CO. The authors gratefully acknowledge useful discussions with Frank Ham, Sanjeeb Bose and Christopher Ivey.

References

- [1] K. Ambo, H. Nagaoka, D. A. Philips, C. Ivey, G. A. Brès, and S. T. Bose. Aerodynamic force prediction of the laminar to turbulent flow transition around the front bumper of the vehicle using dynamic-slip wall model les. *AIAA Paper*, 2018(3302), 2020.
- [2] Matthew Aultman, Zhenyu Wang, Rodrigo Auza-Gutierrez, and Lian Duan. Evaluation of cfd methodologies for prediction of flows around simplified and complex automotive models. *Computers & Fluids*, 236:105297, 2022.
- [3] M. Benjamin, E. Saetta, C. Ivey, S. Bose, F. Ham, and G. Iaccarino. Parametric representation and surrogate modeling of drag for a realistic automotive geometry. *Center for Turbulence Research Annual Research Briefs*, 2023.
- [4] Sanjeeb T. Bose and George Ilhwan Park. Wall-modeled large-eddy simulation for complex turbulent flows. *Annual Review of Fluid Mechanics*, 50:535–561, 2018.
- [5] G. Brès, S. Bose, M. Emory, F. Ham, O. Schmidt, G. Rigas, and T. Colonius. Large-eddy simulations of co-annular turbulent jet using a voronoi- based mesh generation framework. *AIAA Paper*, 2018(3302), 2018.

- [6] A. X. Chang, T. Funkhouser, L. Guibas, P. Hanrahan, Q. Huang, Z. Li, S. Savarese, M. Savva, S. Song, H. Su, J. Xiao, L. Yi, and F. Yu. Shapenet: an information-rich 3d model repository. *arXiv Preprint*, arXiv:1512.03012, 2015.
- [7] Jack Choquette. Nvidia hopper h100 gpu: Scaling performance. *IEEE Micro*, 43(3):9–17, 2023.
- [8] Mohamed Elrefaie, Angela Dai, and Faez Ahmed. Drivaernet: A parametric car dataset for data-driven aerodynamic design and graph-based drag prediction, 2024.
- [9] Roberto Garcia-Fernandez, Koldo Portal-Porras, Oscar Irigaray, Zugatz Ansa, and Unai Fernandez-Gamiz. Cnn-based flow field prediction for bus aerodynamics analysis. *Scientific Reports*, 13(1):21213, December 2023.
- [10] K. A. Goc, O. Lehmkuhl, G. I. Park, S. T. Bose, and P. Moin. Large eddy simulation of aircraft at affordable cost: a milestone in computational fluid dynamics. *Flow*, 1:E14, 2021.
- [11] Erkan Gumpinar, Umut Can Coskun, Mustafa Ozsipahi, and Serkan Gumpinar. A generative design and drag coefficient prediction system for sedan car side silhouettes based on computational fluid dynamics. *Computer-Aided Design*, 111:65–79, 2019.
- [12] Wenchong He, Zhe Jiang, Tingsong Xiao, Zelin Xu, and Yukun Li. A survey on uncertainty quantification methods for deep learning, 2024.
- [13] A. Heft, T. Indinger, and N. Adams. Introduction of a new realistic generic car model for aerodynamic investigations. In *SAE Tech. Paper*, volume 2012-01-0168, 2012.
- [14] Zongyi Li, Nikola B. Kovachki, Kamyar Azizzadenesheli, Burigede Liu, Kaushik Bhattacharya, Andrew M. Stuart, and Anima Anandkumar. Fourier neural operator for parametric partial differential equations. *CoRR*, abs/2010.08895, 2020.
- [15] Zongyi Li, Nikola Borislavov Kovachki, Chris Choy, Boyi Li, Jean Kossaifi, Shourya Prakash Otta, Mohammad Amin Nabian, Maximilian Stadler, Christian Hundt, Kamyar Azizzadenesheli, and Anima Anandkumar. Geometry-informed neural operator for large-scale 3d pdes. In *Proceedings of the 37th Conference on Neural Information Processing Systems (NeurIPS 2023)*. NVIDIA, 2023.
- [16] William E. Lorensen and Harvey E. Cline. Marching cubes: A high resolution 3d surface construction algorithm. In *Proceedings of the 14th Annual Conference on Computer Graphics and Interactive Techniques*, page 163–169. Association for Computing Machinery, 1987.
- [17] Tomas Möller and Ben Trumbore. Fast, minimum storage ray/triangle intersection. In *ACM SIGGRAPH 2005 Courses*, pages 7–es. Association for Computing Machinery, 2005.
- [18] Keiron O’Shea and Ryan Nash. An introduction to convolutional neural networks. *CoRR*, abs/1511.08458, 2015.
- [19] Robert Palin, Vincent Johnston, Shaun Johnson, Andrew D’Hooge, Bradley Duncan, and Joaquin Gargoloff. The aerodynamic development of the tesla model s - part 1: Overview. 04 2012.
- [20] Olaf Ronneberger, Philipp Fischer, and Thomas Brox. U-net: Convolutional networks for biomedical image segmentation. *CoRR*, abs/1505.04597, 2015.
- [21] Ettore Saetta, Renato Tognaccini, and Gianluca Iaccarino. Machine learning to predict aerodynamic stall. *International Journal of Computational Fluid Dynamics*, 36(7):641–654, August 2022.
- [22] Ettore Saetta, Renato Tognaccini, and Gianluca Iaccarino. Uncertainty quantification in autoencoders predictions: Applications in aerodynamics. *Journal of Computational Physics*, 506:112951, 2024.
- [23] B. Song, C. Yuan, F. Permenter, N. Arechiga, and F. Ahmed. Surrogate modeling of car drag coefficient with depth and normal renderings. *arXiv Preprint*, arXiv:2306.06110, 2023.

- [24] Olga Sorkine. Laplacian Mesh Processing. In Yiorgos Chrysanthou and Marcus Magnor, editors, *Eurographics 2005 - State of the Art Reports*. The Eurographics Association, 2005.
- [25] Nobuyuki Umetani and Bernd Bickel. Learning three-dimensional flow for interactive aerodynamic design. *ACM Trans. Graph.*, 37(4), jul 2018.
- [26] Jonathan Viquerat and Elie Hachem. A supervised neural network for drag prediction of arbitrary 2d shapes in laminar flows at low reynolds number. *Computers and Fluids*, 210:104645, 2020.
- [27] Christopher Williams and Carl Rasmussen. Gaussian processes for regression. In D. Touretzky, M.C. Mozer, and M. Hasselmo, editors, *Advances in Neural Information Processing Systems*, volume 8. MIT Press, 1995.
- [28] Guoping Xu, Xiaxia Wang, Xinglong Wu, Xuesong Leng, and Yongchao Xu. Development of skip connection in deep neural networks for computer vision and medical image analysis: A survey, 2024.